

PAPER DETAILS

TITLE: Effects of Mechanical Milling and FAST on Mg Powders: Microstructural Analysis and Mechanical Properties

AUTHORS: Yasemin Yahsi,Rasim Ipek

PAGES: 1436-1449

ORIGINAL PDF URL: <https://dergipark.org.tr/tr/download/article-file/3458952>



Effects of Mechanical Milling and FAST on Mg Powders: Microstructural Analysis and Mechanical Properties

Yasemin YAHSI^{1, 2, *} , Rasim IPEK² 

¹Dokuz Eylül University, Bergama Vocational School, İzmir, Türkiye

²Ege University, Mechanical Engineering Department, İzmir, Türkiye

Highlights

- The effect of mechanical milling and sintering parameters on Mg powders sintered using FAST.
- Effect of particle properties of mechanically milled Mg on microstructure and FAST mechanism.
- The effect of mechanical milling and FAST parameters on compressive strength and hardness of Mg.

Article Info

Received: 06 Oct 2023

Accepted: 13 Jan 2024

Keywords

Mechanical milling
Mechanical activation
FAST
Sintering mechanism
Magnesium

Abstract

This study investigates the sintering mechanism of commercially pure Magnesium (Mg) using the Field Assisted Sintering Technique (FAST). Powder morphologies are in a vast variety of spherical to flake, as well as nano to fine grain as in powder size and mechanically milled (MM) between 0-108 hours. The MM'ed Mg particles were sintered by FAST with at 350-425°C for 5-20min. Relative densities (93-99%) and compressive strength up to 369MPa were obtained from FAST'ed Mg samples depending on MM durations and particle geometries which significantly influenced the sintering mechanism. SEM and XRD analysis identified four distinct bonding and sintering mechanisms influenced by particle geometry, residual stress, and microstructure developed through mechanical milling. The combination of mechanical milling and FAST exhibited significant effects on the microstructural and mechanical properties of Mg powders, with the Mg₃₆ sample displaying promising strength and hardness.

1. INTRODUCTION

Powder metallurgy is one of the most characterizable metal manufacturing methods due to sintering parameters. These parameters are sintering time, temperature and compaction pressure. In the field assisted sintering technique (FAST), electric current is used simultaneously with compression pressure. This ensures extremely high heating rates and short processing times [1]. FAST is a mostly low voltage, pulsed direct current (DC), pressure-assisted sintering technique, which has been widely applied for materials processing in recent years' studies [2]. This concept is a sintering technique, which has been increasingly used for the sintering of a variety of materials with nano-sized grains to achieve superior properties. Compared to conventional pressing and sintering, conventional hot pressing or hot isostatic pressing, field assisted sintering has resulted in many improvements in mechanical properties [3]. According to Shen et al. in their work in 2002, they used parameters such as sintering time and temperature to minimize grain growth and increase the mechanical properties in this way [4]. Guillon et al, stated that in their work in 2014, FAST methods use less time and temperature to sinter the powders compared to the conventional sintering methods. This means less energy and less cost comparison with conventional sintering [5].

It has been determined that atomic level diffusion mechanisms are more effective than surface diffusion in the early stages of sintering, as high defect rates increase at high heating rates and grain growth is inhibited [6]. High heating rates increase surface diffusion in the early stages of sintering, thereby increasing the compaction rate of powder compacts and limits the grain growth. Olevsky et al, indicates that rapid heating

* Corresponding author, e-mail: yasemin.yahsi@deu.edu.tr

increases the sinterability of powder particles, temperature gradient is higher at the powder compaction nodes also inducing the necking and neck growth of the powders [7]. This phenomenon also causes highly nonuniform mechanical properties such as residual stresses and dislocation creep distributions.

Local temperature gradients are caused by the thermal diffusion of void spaces; macroscopic temperature gradients cause thermal stresses. Thermal gradient creates higher thermal stress in porous structure. Although thermal stress alone does not cause (independent) macroscopic volume reduction, we contribute to both the formation and movement processes of dislocations by increasing the diffusion rates during sintering as well as plastic deformation [2].

With conventional sintering (JH or external heating), sintering is done at low speeds. Necking is a typical conventional sintering mechanism based on surface diffusion. It can be defined by the micro-defects that remain between the spherical powders in the microstructure. As mentioned, surface diffusion is suppressed as FAST sintering takes place with high heating rates. Therefore, different diffusion mechanisms are also involved in FAST [8].

Mechanical milling (MM) is a process in which the powders are blended, cold worked, welded and broken [9]. With a high energy ball milling process, powders with uniform atom distribution are created in a thinner microstructure in stable or metastable phase [10]. The function of mechanical milling is to create an amorphous material by completely destroying the crystal structure by creating point defects and lattice defects (e.g. cavities, dislocations, etc.) [11]. The MM process constantly creates new surfaces in the Mg particles. When clean surfaces come into contact, they provide fast diffusion conditions. It also provides powder formation in various shapes and sizes [12]. Also, mechanical milling has been known to be an effective processing technique for producing nanocrystalline metals [13]. In mechanical milling, factors such as powder/ball ratio, milling time and speed, must be controlled since they affect the properties of the resulting materials [14,15].

Hwang et al, indicates that during the MM process, powder particles undergo plastic deformation with high strain rates. Thus, producing complex, dense networks of dislocations and keeping strain energy remains in the particles [13]. At the same time, according to Yahşi and İpek, with plastic deformation, the oxide layers on the surfaces of the powders begin to break and shell out so that the powders are mechanically activated [16]. However, these gains can be lost in classical sintering. The search for low-energy rapid sintering continues to preserve the gains. With FAST, these gains can be partially preserved. Magnesium (Mg) is one of the lightest structural metals with a density of 1.738 g/cm^3 [17]. Mg is the third most-commonly used structural-metal, after steel and aluminum. Mg and Mg alloys are well known as lightweight construction materials and are finding more and more applications in end user products and industrial parts. Due to their light weight, Mg alloys have been increasingly used in the automotive, aerospace, electronics industry in recent years. Mg is also used in biodegradability applications of implants and stents. Sealy et al. 2016 used magnesium as a biodegradable stent material in their research. Therefore, although Mg and Mg alloys have these advantageous properties, their relatively low ductility limits their applicability in large areas as a high-performance structural material [18]. According to Friedrich and Mordike, Mg has low density, stiffness, high damping capacity, bending resistance and specific strength [17]. In addition, Mg has low plastic deformation at room temperature due to the few sliding systems exhibited by the Hexagonal Close Packed (HCP) structure [19]. To overcome poor formability and mechanical performance of Mg, powder metallurgy production method (PM) can be used. PM technique is commonly used to produce Mg and Mg based parts. PM methods can improve mechanical properties by adjusting the sintering parameters.

Zhuang et al. revealed that the microstructural and mechanical properties of porous magnesium produced by PM are affected by the total porosity, pore size, distribution and shape, and the connection between magnesium powders [20]. These properties can be modified by selecting the sintering time, sintering temperature, compacting pressure, shape of the starting material powders. According to Yamashita et al., grain coarsening of the Mg particle during the sintering process can also affect the microstructural and mechanical properties of the final material [21]. MM was used to change the shape of starting material in this study. After the MM process, the sintering process was applied to the powders. FAST was used for the

sintering process in order to maintain the mechanical milling gains as much as possible. This study was designed with the assumption that another dynamic of these diffusion mechanisms would be related to powder geometry and microstructure. The FAST-sintering mechanism formed between the powders mechanically activated by MM and having spherical-like, flake-like geometries with MM effect was investigated. MM was applied to Mg powders for different times. The effect of different milling times on Mg powders is especially investigated.

In the present work, the combined effects of mechanical milling time, sintering temperature, sintering time; on Brinell hardness and compressive strength were investigated. Statistical experiment design and analysis were performed using Central Composite Design (CCD) in response surface methodology (RSM). According to Myers et al., RSM consists of statistical and mathematical techniques used to analyze the effects of several independent variables [22]. RSM helps to investigate the interactive effect of experimental variables and provides a mathematical model that can provide information about the overall process. According to research by Ferreira et al., CCD is one of the most efficient and common designs used in response surface modeling [23]. To evaluate the significance of the model, experimental data were analyzed by performing Analysis of Variance (ANOVA).

The primary objective of this study is to examine the influence of mechanical milling time on the sintering properties of Magnesium metal, considering various parameters including sintering temperature and sintering time.

2. MATERIAL METHOD

Mg powders were obtained from Kumas Manyezit Sanayi A.S. (Kütahya, Türkiye). The purity of Mg is $\geq 99.3\%$, its size is ≤ 220 . Zinc Stearate ($C_{36}H_{70}O_4Zn$) was used as a process control agent. Zinc was used at 1% by weight of magnesium powder.

2.1. Powder Milling and Sintering

Mg powders were milled by high energy ball milling. Planetary ball mill was used as ball miller (DECO-PBM-V-2L). Milling containers were treated in the glovebox under Argon protective atmosphere. The milling balls used are stainless steel with a diameter of 10 mm [24]. The ball-to-powder ratio was 20:1. Ball milling was carried out at 160 rpm.

The original electric resistance sintering device, known as electricity field assisted sintering (FAST), was utilized for the sintering process. The FAST device operates through the use of AC circuits and low current, while an external joule heating technique is facilitated by a graphite die. The application of the graphite die, standing at a height of 50 mm, alongside punches measuring 10 mm in diameter and 20 mm in height, allowed for sintering to take place in an Argon atmosphere. A pressure of 45 MPa was applied utilizing a graphite mold within a uniaxial FAST machine. The sintering temperature ranged from 383 to 467 °C in an Argon atmosphere, which was assisted by a vacuum. The sintering cycle encompassed a 5-minute warm-up phase, followed by waiting periods of 7, 10, 15, 20 and 23 minutes, concluding with a 5-minute cool-down phase. A diagram of the FAST sintering machine can be found in Figure 1.

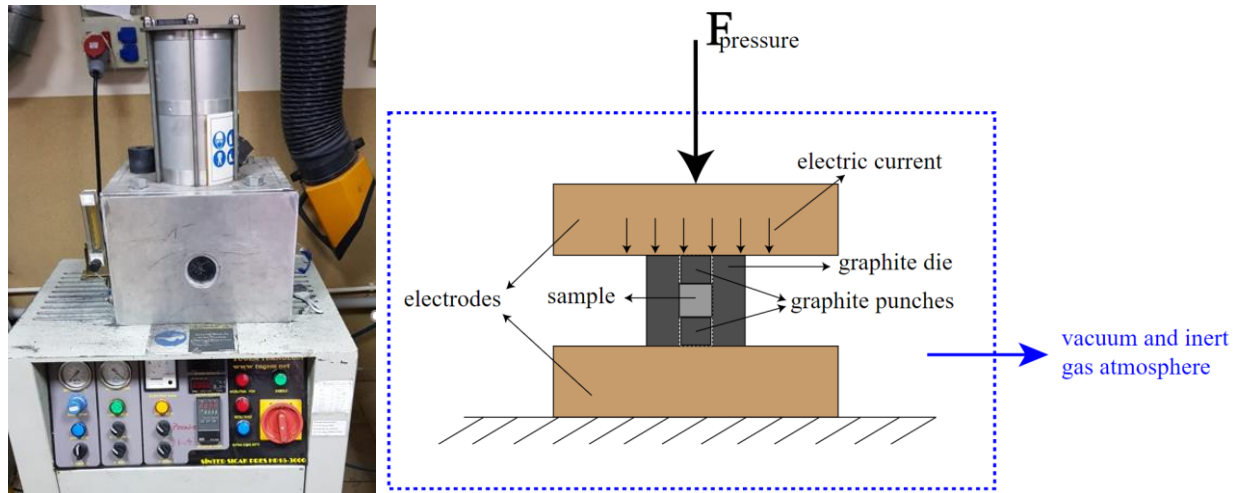


Figure 1. FAST sintering machine and diagram

2.2. SEM, XRD and EDS Analysis, Compressive Strength and Hardness Tests

SEM imaging was conducted using the Thermo Scientific Apreo S Scanning Electron Microscope, utilizing backscattered electrons.

EDS analysis was performed in conjunction with SEM imaging to obtain elemental composition information. XRD analysis was carried out on the Thermoscientific ARL X'TRA X-Ray Diffractometer (ISDD standard cart number 01-089-4244), covering a diffraction angle range of 5° to 85° .

Compressive strength tests were conducted using a Shimadzu (AG-IS 100 kN) tensile-compression tester at a constant speed of 0.2 mm/min. Hardness tests were performed on the Brinell scale, with measurements obtained using a load of 62.5 kgf and a 30-second waiting time.

2.3. Experimental Design

Central Composite Design (CCD) statistical experiment design and the response surface methodology were employed to investigate the effects of the four independent variables on the response function. CCD was applied to determine the optimum process variables for Sintered Magnesium. CCD was also used to obtain a model that required a minimum number of experiments. The independent variables were milling time (A), temperature (B) and sintering time (C). The low and high levels of each variable are designated as -1 and +1, respectively as illustrated in Table 1. The experimental levels for all variables were selected based on results from preliminary experiments.

Table 1. Independent variables and their levels used for CCD

Independent Variables	Unit	Factor's Symbol	Coded Levels	
			-1	1
Milling time	h	A	36	90
Temperature	$^\circ\text{C}$	B	400	450
Sintering time	min	C	10	20

3. THE RESEARCH FINDINGS AND DISCUSSION

3.1. Model Fitting

A total of 20 experiments have been employed in this work to evaluate the effects of the three main independent parameters on compressive strength, Brinell hardness. For powders obtained by mechanical

milling process; average diameters (D_0), the ratio of the smallest width to the largest width (d_s/d_l) measured on the powders are given in Table 2. These values are measured by using image process technique. Table 2 also shows the experimental design matrix results (sintering parameters, compression strength and hardness values) and sample densities.

Table 2. Mg powder and sintered sample values after mechanical milling process

Milling Time (h)	D_0 (μm)	Particle Size (d_s/d_l)	Sintering time/temperature		Compressive Strength (MPa)	Hardness (HB)	Density (%)
			min	$^{\circ}\text{C}$			
0	47	0.52	15 \pm 5	425 \pm 25	195 \pm 20	55 \pm 4	96 \pm 0.4
18	34	0.91			270 \pm 30	76 \pm 2	99 \pm 0.5
36	50	0.47			300 \pm 65	55 \pm 5	97.8 \pm 1
63	36	0.89			260 \pm 30	84 \pm 5	96 \pm 0.3
90	23	0.92			195 \pm 35	85 \pm 7	95 \pm 0.6
108	20	0.98			140 \pm 5	91 \pm 5	93.8 \pm 0.1

The factors considered on compressive strength are shown using a perturbation plot (Figure 2). The slope of the milling time (A), the temperature (B) and the sintering time (C) shows the severity of its influence on the compressive strength.

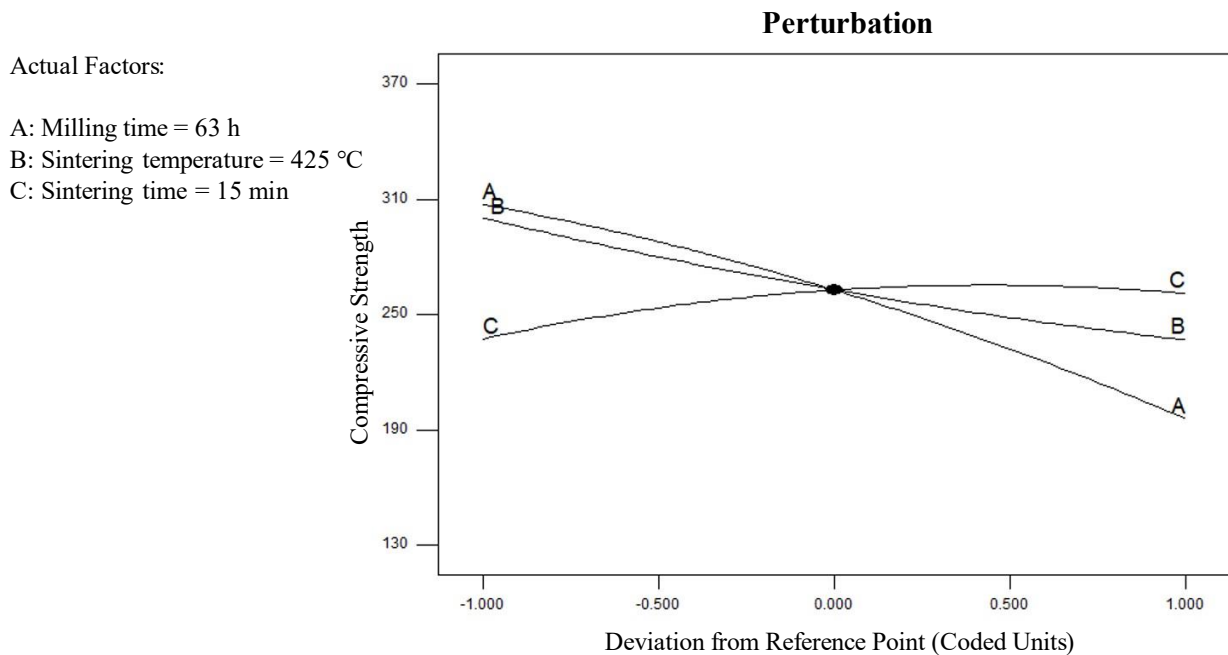


Figure 2. Perturbation plot of compressive strength

The regression model for compressive strength (Y_1) is given in Equation (1), after insignificant terms are discarded

$$Y_1 \text{ (MPa)} = +262.73 - 55.74 * A - 31.64 * B + 11.80 * C + 12.66 * A * B + 4.94 * A * C + 10.49 * B * C - 11.39 * A^2 + 5.70 * B^2 - 13.57 * C^2 - 11.89 * A * B * C. \quad (1)$$

In this study, the highest compressive strength among the samples is Mg_{36} with 368 MPa and the lowest compressive strength to Mg_{108} with 140 MPa.

The hardness test results are given in the perturbation graph in Figure 3.

Actual Factors:

A: Milling time = 63 h

B: Sintering temperature = 425 °C

C: Sintering time = 15 min

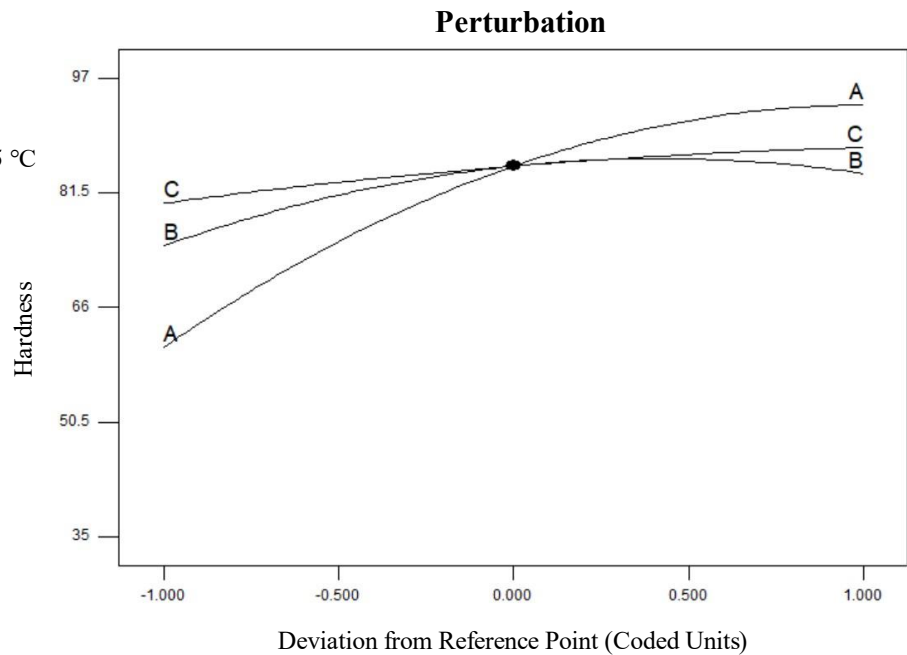


Figure 3. Perturbation plot of hardness

After insignificant terms discarded, the regression equation can be shown in Equation (2) for hardness (Y_2)

$$Y_2 \text{ (HB)} = +85.13 + 16.38 * A + 4.90 * B + 3.75 * C + 2.50 * A * B + 0.25 * B * C - 8.12 * A^2 - 5.87 * B^2 - 1.25 * C^2 \quad (2)$$

In this study, sintering temperature and time as a variation were chosen relatively narrow to observe the effect of MM on powder geometry. The compression and hardness test results given in Table 2 are consistent with the results of Figures 2, Y_1 , Figure 3 and Y_2 , confirming that the MM time is more effective than the selected sintering temperature and time. For this reason, the effect of sintering variables in the selected values is limited and negligible.

3.2. XRD Results

The XRD analysis of Mg powders MM'ed for 18 hours, 36 hours, 63 hours, 90 hours and 108 hours are given at Figure 4.

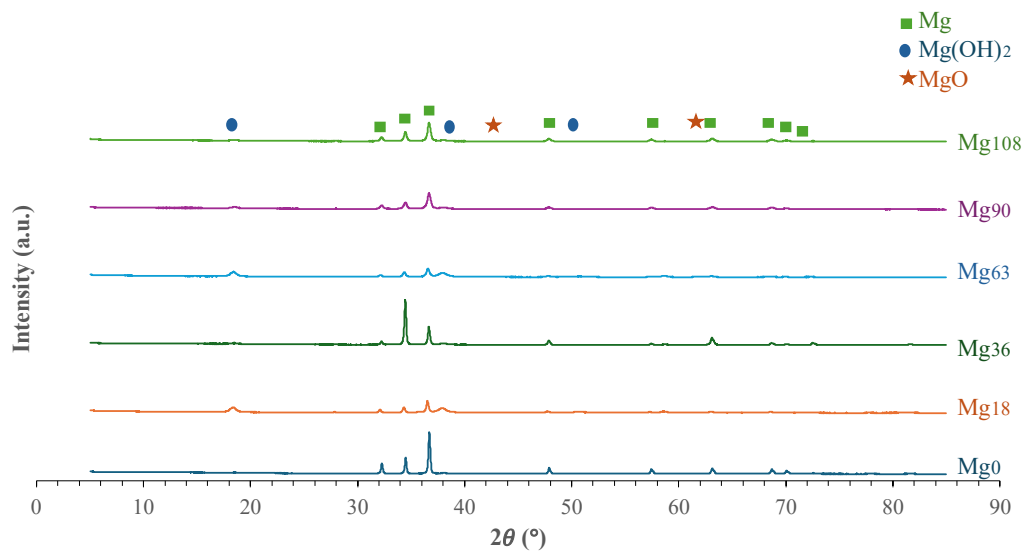


Figure 4. XRD results

The results of The XRD's show that the sample MM'ed for 36 h was quite different from other one as well as apparent density and average particle diameters.

For Mg powder MM'ed 36h, XRD results show that the maximum peak (dominant atomic array) takes place at 34.4 instead of 36.5 degrees which is an ordinary position. At this point, the intensity of the peak is also very high. It seems that the results for the others MM'ed powder samples are almost parallel to expectations and not any surprise except 36h MM'ed.

Lattice micro-strain and crystal size were obtained by Scherrer equation (Equation (3) and (4)) [25]:

$$\beta = \frac{K\lambda}{L\cos\theta} \quad (3)$$

$$\beta = C\varepsilon \frac{\sin\theta}{\cos\theta}. \quad (4)$$

β is the peak width, consists of the contribution of the crystallite size L and the lattice micro-strain ε . K is the Scherrer constant, assumed to be around 1. λ is the wavelength of X-ray. ε is the inhomogeneous strain. The value of the constant C is typically 4. The full width at half maximum (FWHM) is the width of the diffraction peak at half of its maximum amplitude.

Crystal size and lattice microstrain values are given in Table 3.

Table 3. Crystal size and lattice microstrain values

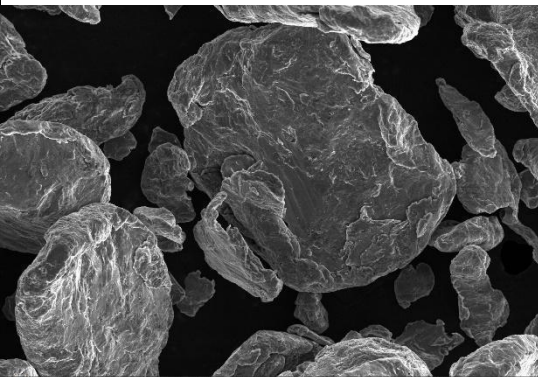
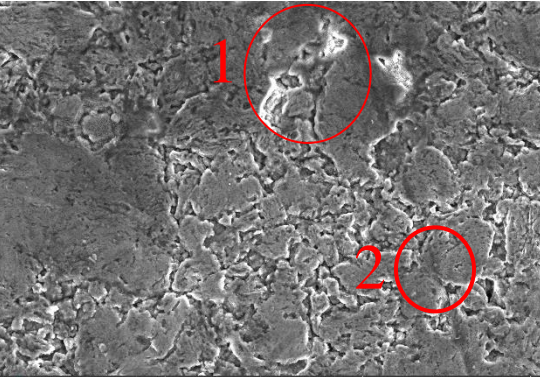
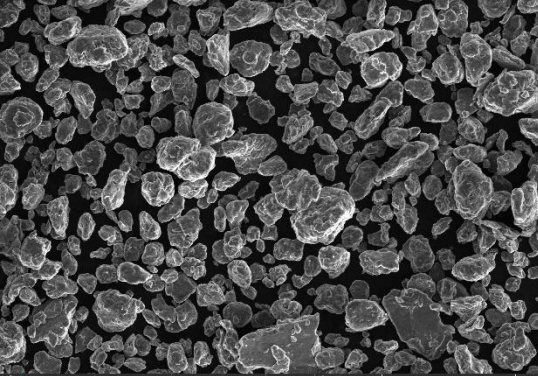

Milling Time (h)	Crystal Size (nm)	Lattice Microstrain (%)
0	672	0.13
18	18	1.14
36	17	0.09
63	110	0.24
90	16	0.16

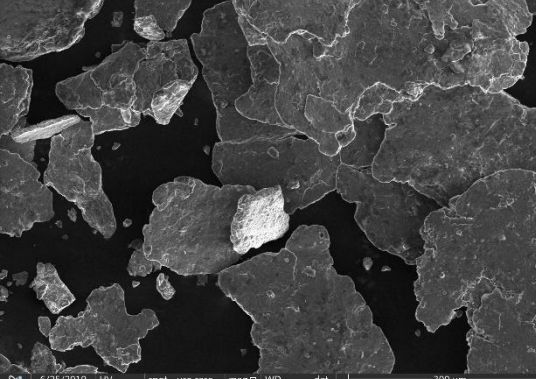
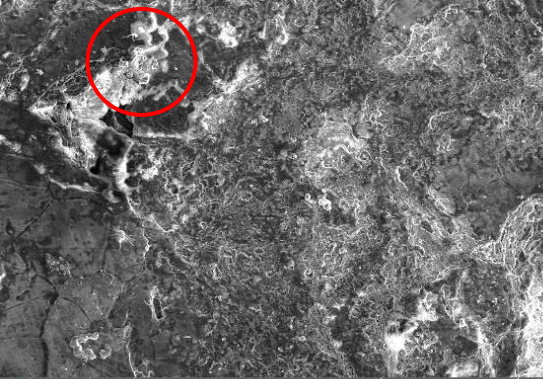
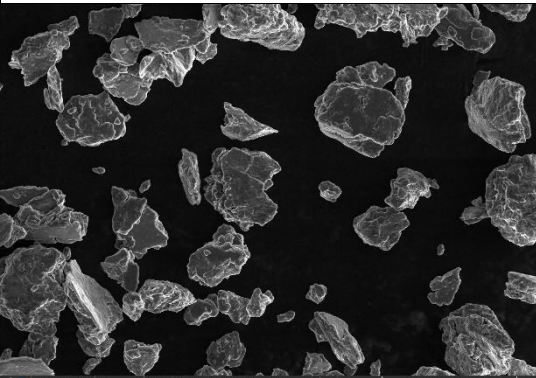
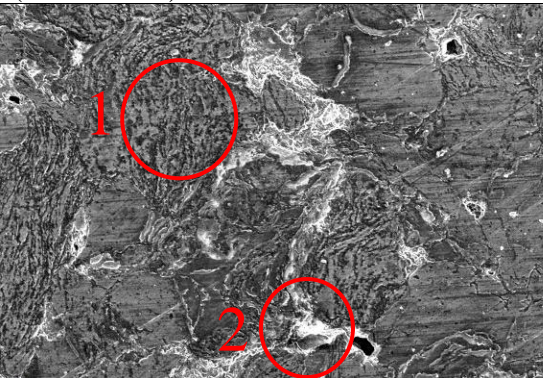
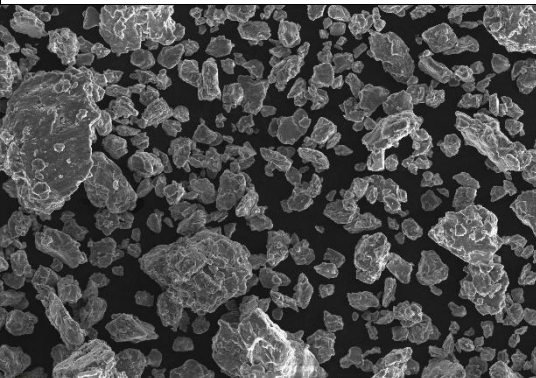
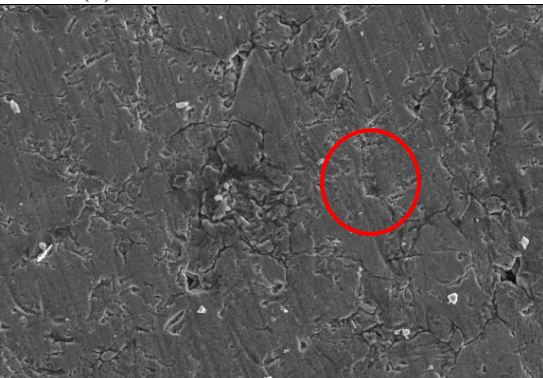
108	19	0.006
-----	----	-------

In the MM'ed Mg samples, an increase in broadening and a decrease in intensity were observed with increasing MM time, which can be attributed to microstructural changes such as grain refining, recovery, and/or recrystallization. However, according to the literature, it is stated that the crystal size cannot be smaller than 20 nm. The Mg₆₃ XRD result revealed a significant difference in average grain diameters with 110 nm, likely due to the stacking of flake layers. A comparison of XRD peaks between Mg₃₆ and Mg₁₈ revealed a transition from high to low strain values, indicating a change in microstructure at the crystal level. This suggests that Mg strains are too high in the previous stage to become flakes, resulting in a change in the crystal level.

3.3. SEM Images of Mechanically Milled Mg Powders and FAST-Sintered Samples

The SEM images of the Mg powder samples subjected to mechanical milling (MM'ed) for different durations (ranging from 0 to 108 hours) and subsequently sintered using FAST are presented in Table 1. The milling process resulted in diverse particle geometries, ranging from nearly spherical to flake-like structures, accompanied by variations in particle and grain sizes. The observed changes, particularly the alteration in particle geometry, were found to exert a significant influence on the sintering mechanisms (Figure 5).

<p>a</p> <p>Mg₀</p>	 <p>$D_o=54\text{ }\mu\text{m}$, $d_s/d_l=0.52$</p>	 <p>425°C, 15min, 192MPa, 96% Necking(2) and partially FAST effect(1)</p>
<p>b</p> <p>Mg₁₈</p>	 <p>$D_o=34\text{ }\mu\text{m}$, $d_s/d_l=0.91$</p>	 <p>425°C, 15min, 307MPa, 99% (Necking effect)</p>

<p>c</p> <p>Mg₃₆</p>	 <p>6/25/2019 HV spot use case mag WD det 11:10:19 AM 10.00 kV 9.0 Standard 500 x 10.0 mm ETD</p> <p>$D_o=50\text{ }\mu\text{m}$, $d_s/d_l=0.47$</p>	 <p>1/14/2019 HV spot use case mag WD det 9:19:19 AM 5.00 kV 8.0 Standard 2 000 x 9.3 mm ETD</p> <p>400°C, 10min, 369MPa, 97.8 % (FAST effect)</p>
<p>d</p> <p>Mg₆₃</p>	 <p>6/25/2019 HV spot use case mag WD det 10:58:16 AM 10.00 kV 9.0 Standard 1 000 x 9.9 mm ETD</p> <p>$D_o=36\text{ }\mu\text{m}$, $d_s/d_l=0.89$</p>	 <p>1/14/2019 HV spot use case mag WD det 9:38:21 AM 5.00 kV 8.0 Standard 2 000 x 11.9 mm ETD</p> <p>383°C, 15min, 320MPa, 96% Sandwich effect(1) and partially FAST effect(2)</p>
<p>e</p> <p>Mg₉₀</p>	 <p>6/25/2019 HV spot use case mag WD det 10:30:06 AM 10.00 kV 9.0 Standard 1 000 x 10.0 mm ETD</p> <p>$D_o=23\text{ }\mu\text{m}$ $d_s/d_l=0.92$</p>	 <p>1/14/2019 HV spot use case mag WD det 8:57:10 AM 10.00 kV 8.0 Standard 2 000 x 11.8 mm ETD</p> <p>400°C, 20min, 231MPa, 95% (Necking effect)</p>

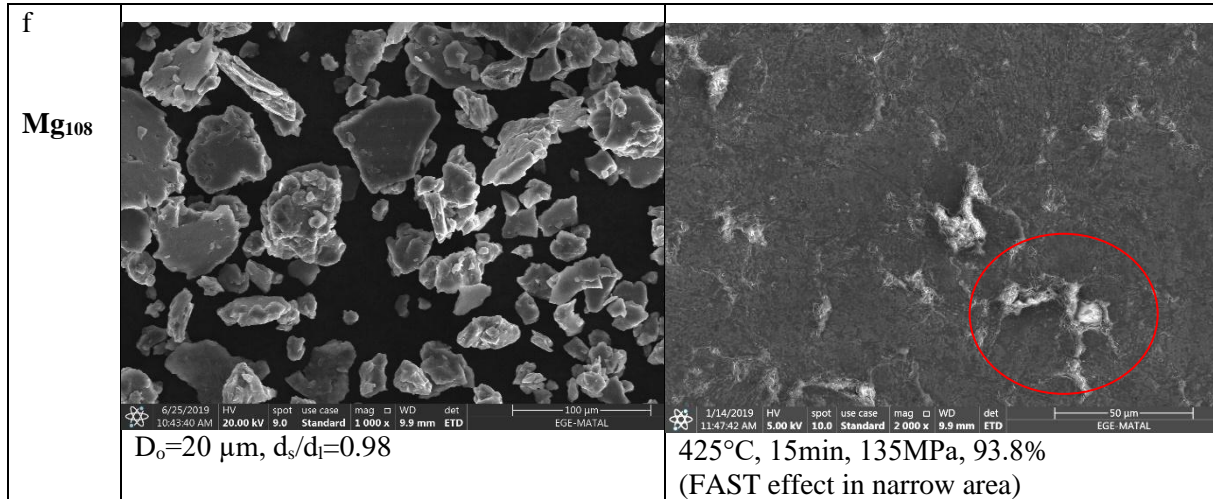


Figure 5. Scanning electron microscope images of of Mg powders subjected to specific durations of mechanical milling (MM). The images include the following: a) Mg powders without MM process (Mg), b) Mg powders MM'ed for 18 hours (Mg_{18}), c) Mg powders MM'ed for 36 hours (Mg_{36}), d) Mg powders MM'ed for 63 hours (Mg_{63}), e) Mg powders MM'ed for 90 hours (Mg_{90}), and f) Mg powders MM'ed for 108 hours (Mg_{108}), (D_0 is an arithmetic average diameter and d_s/d_l is the ratio of the smallest width to the greatest width)

The SEM analysis revealed notable changes in particle size and shape with respect to milling time. The average diameter of the particles, referred to as d_0 , exhibited a decrease from $54\ \mu\text{m}$ to $20\ \mu\text{m}$ as the milling time progressed. The initial morphology of Mg particles (Mg) appeared irregular, as observed in Figure 5a. In Figure 5b, Mg_{18} exhibited a more spherical form, although it was observed to be mixed with particles of different geometries. Mg_{108} and Mg_{90} exhibited a predominantly spherical shape, while Mg_{36} displayed a flaky morphology (Figure 5c, f). Mg_{63} appeared to be a mixture of like-spherical and flaky particles, suggesting a composition of Mg_{90} and Mg_{36} powders. Additionally, the particle sizes were categorized into large and small ranges. The average particle size of Mg_{63} powder ($\approx 36\ \mu\text{m}$) is similar to Mg_{18} ($\approx 34\ \mu\text{m}$), but the standard deviations of particle size for Mg_{63} are lower. Mg_{18} and Mg_{90} powders have similar like-spherical shapes in SEM photos, but they differ in size and dimensions. Mg_{18} has larger dimensions ($34\ \mu\text{m}$) than Mg_{90} ($23\ \mu\text{m}$) (SEM Figure 5, b, e), and there are significant differences in XRD patterns. Mg_{108} powders resemble Mg_{90} in XRD results, but Mg_{108} tends to transform from like-spherical to flaky geometry ($d_s/d_l \approx 0.93$) and shows less homogeneity compared to Mg_{90} . The SEM observations clearly indicate the formation of Mg powders with varying sizes and shapes at different milling times. A distinctive pattern emerges, wherein the shape transitions cyclically from like-spherical to flaky and then reverts back to like-spherical. Notably, despite the resemblance in shape, the particle size exhibits significant variations at each stage, depending on the milling time. Moreover, these powders exhibit discernible differences in their microstructural properties, as evidenced by XRD analysis.

3.4. SEM Analysis of FAST-Sintered Samples

The microstructure of all sintered samples is depicted in Figure 5 through SEM images. Notably, significant variations exist among their sintering mechanisms. SEM images vividly demonstrate the occurrence of key sintering mechanisms, such as mechanical locking, necking, sandwich effect, and the characteristic FAST path (White Bright Path-WBP). These mechanisms are influenced by the powder geometry and particle microstructure properties, as clearly observed in Figure 5.

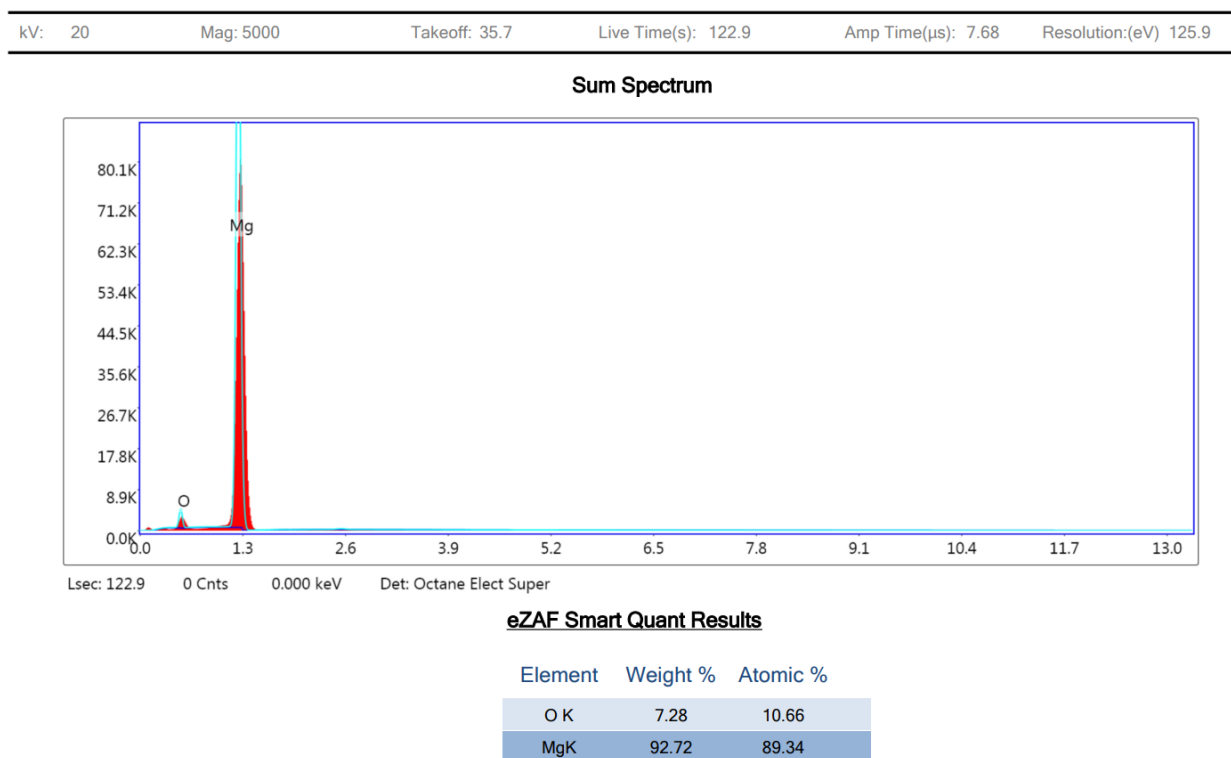
Necking is a well-known sintering mechanism, primarily driven by surface diffusion and influenced by variables such as contact surface, temperature, and time. In the case of the electric field-assisted sintering technique (FAST), bonding occurs at the atomic level, involving atomic defects, grain boundaries, and electromigration, in addition to necking [26]. The mechanisms of FAST are largely influenced by process variables, including circuit current, voltage, and conductivity [20]. The microstructure exhibits a light white path (WBP), characterized by a high short-current pass path. Within the WBP, the high short-current

induces partial melting, deoxygenation, and the formation of liquid splashes due to arc formation and its vicinity, along with the effects of joule heating (JH). The necking mechanism, a classical sintering process, is prominently observed in the microstructure of sintered Mg, Mg₁₈, and Mg₉₀ particles, as indicated by SEM analysis (Figure 5). The nearly spherical shape and compact arrangement of these particles facilitate strong interparticle contact and stability during sintering (Figure 5b, e).

Conversely, the presence of distinct FAST tracks or widespread white bright path (WBP) is not evident in these samples. The dominance of necking as the primary sintering mechanism for Mg can be attributed to its lack of mechanical activation, which aligns with the characteristics of FAST. In the case of sintered flaky Mg₃₆ powders (Figure 5c), the microstructure exhibits mechanical locking sintering and the presence of a white light path (WBP) with an intensity of 0.47. Similarly, the sintered Mg₆₃ sample with d_s/d_l 0.92 reveals clear indications of WBP, mechanical locking, and a sandwiched structure (Figure 5d). A narrow region in the microstructure of the Mg₁₀₈ sample sintered with d_s/d_l 0.93 shows a few bright points suggestive of WBP, but no significant traces of sandwich formation are observed.

3.5. Mechanical Analysis Results

The mechanical test results, including compression strength, hardness, and percent full density, were observed to be influenced by the mechanical activity of the powder and its geometry for all MM'ed samples, except for Mg₁₀₈, which exhibited high levels of oxidation in its structure (Figure 6, EDS analysis). Among the samples, Mg₃₆ demonstrated the highest compression strength, attributed to its mechanically activated structure and particle shapes that are well-suited for FAST sintering. In contrast, the Mg₁₀₈ sintered sample exhibited a significantly lower density rate of 0.94 and a compressive strength of 135 MPa, with no apparent signs of plastic deformation in the sintered microstructure. The EDS analysis suggests that the high oxygen content in Mg₁₀₈ may have negatively impacted the bonding process. Refer to Figure 6 for the EDS analysis of the sintered sample.



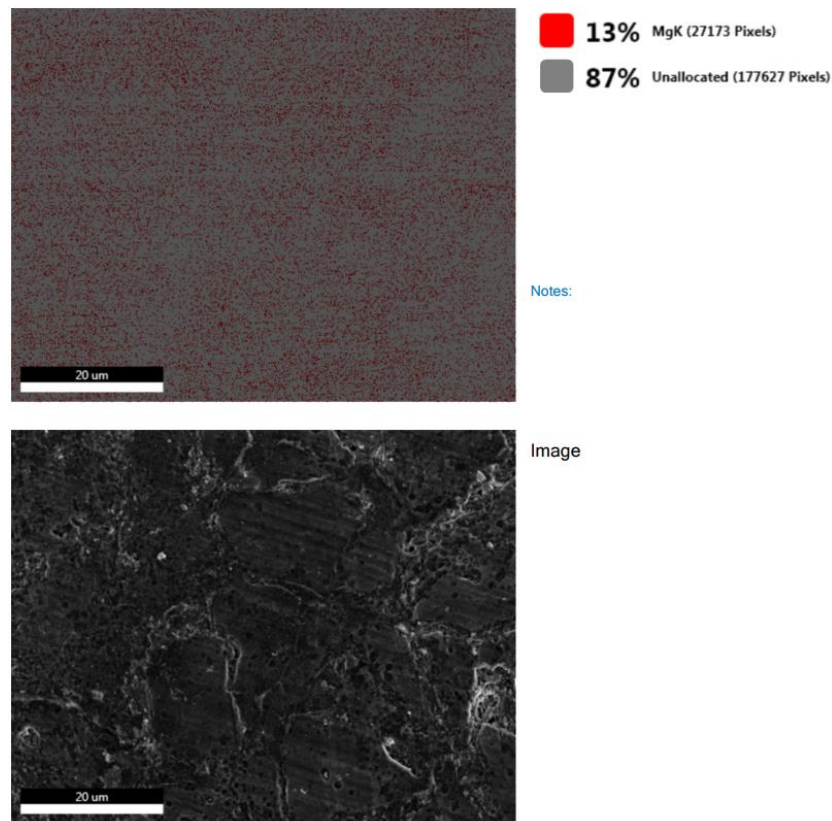


Figure 6. EDS analysis of the sintered sample

4. CONCLUSIONS

The mechanical milling process led to exceptional changes in particle sizes, geometry, and microstructural properties. Particle sizes are decreased, and the shape of the powders approached a near spherical geometry by milling up to 18 hours. From 18 to 36 hours of milling, the powder structure became flaky, and the average particle size increased significantly. The microstructures of sintered samples, specifically Mg₁₈ and Mg₉₀, exhibited homogeneity, whereas Mg₃₆ and Mg₆₃ displayed increased heterogeneity attributed to mechanical locking and FAST induced WBP. The compressive strength increased until the 36 hours of milling time, and then started to decline. Sintered Mg₃₆ had the biggest compressive strength at 369 MPa. Sintered Mg₁₈ samples showed the highest bulk density ratio of 0.99. The increase in temperature, sintering time and milling time had an increasing effect on the hardness values.

CONFLICTS OF INTEREST

No conflict of interest was declared by the authors.

REFERENCES

- [1] Groza, J.R., Garcia, M., Schneider, J.A., “Surface effects in field-assisted sintering”, *Journal of Materials Research*, 16(1): 286-292, (2001).
- [2] Olevsky, E. A., Dudina, D.V., “Field-assisted sintering: Science and applications”, Springer International Publishing, (2018).
- [3] Weston, N. S., Thomas, B., Jackson, M., “Processing metal powders via field assisted sintering technology (FAST): a critical review”, *Materials Science and Technology (United Kingdom)*, 35(11): 1306-1328, (2019).

- [4] Shen, Z., Johnsson, M., Zhao, Z., Nygren, M., “Spark Plasma Sintering of Alumina”, *Journal of the American Ceramic Society*, 85(8): 1921-1927, (2002).
- [5] Guillon, O., Gonzalez-Julian, J., Dargatz, B., Kessel, T., Schierner, G., Räthel, J., Herrmann, M., “Field-assisted sintering technology/spark plasma sintering: Mechanisms, materials, and technology developments”, *Advanced Engineering Materials*, 16(7): 830-849, (2014).
- [6] Tokita, M., “Progress of spark plasma sintering (SPS) method, systems, ceramics applications and industrialization”, *Ceramics*, 4(2): 160-198, (2021).
- [7] Olevsky, E. A., Kandukuri, S., Froyen, L., “Consolidation enhancement in spark-plasma sintering: Impact of high heating rates”, *Journal of Applied Physics*, 102(11), (2007).
- [8] Li, X. Y., Zhang, Z. H., Cheng, X. W., Huo, G. J., Zhang, S. Z., Song, Q., “The development and application of spark plasma sintering technique in advanced metal structure materials: A review”, *Powder Metallurgy and Metal Ceramics*, 60(7–8): 410-438, (2021).
- [9] Murty, B. S., Ranganathan, S. J. M. R., "Novel materials synthesis by mechanical alloying/milling", *International Materials Reviews*, 43(3): 101-141, (1998).
- [10] Schwarz, R. B., Koch, C. C., “Formation of amorphous alloys by the mechanical alloying of crystalline powders of pure metals and powders of intermetallics”, *Applied Physics Letters*, 49(3): 146-148, (1986).
- [11] Suryanarayana, C., “Mechanical alloying and milling”, *Progress in Materials Science*, 46(1-2): 1-184, (2001).
- [12] El-Eskandarany, M. S., “Controlling the powder milling process”, In: *Mechanical Alloying*, 48-83, (2015).
- [13] Hwang, S., Nishimura, C., McCormick, P.G., “Mechanical milling of magnesium powder”, *Materials Science and Engineering A*, 318: 22-33, (2001).
- [14] Rashad, M., Pan, F., Asif, M., “Room temperature mechanical properties of Mg-Cu-Al alloys synthesized using powder metallurgy method”, *Materials Science and Engineering A*, 644: 129-136, (2015).
- [15] Samal, C. P., Parihar, J. S., Chaira, D., “The effect of milling and sintering techniques on mechanical properties of Cu-graphite metal matrix composite prepared by powder metallurgy route”, *Journal of Alloys and Compounds*, 569: 95-101, (2013).
- [16] Yahşi, Y., İpek, R., “Effect of ball milling time on microstructural properties of Mg/MgO”, *Hacettepe Journal of Biology and Chemistry*, 50(3): 269-274, (2022).
- [17] Friedrich, H. E., Mordike, B. L., “Technology of Magnesium and Magnesium Alloys”, In: *Magnesium Technology*, 219-430, 2006.
- [18] Sealy, M. P., Guo, Y. B., Liu, J. F., Li, C., “Pulsed laser cutting of Magnesium-Calcium for biodegradable stents”, in *Procedia CIRP*, 42: 67-72, (2016).
- [19] Barnett, M. R., “Forming of Magnesium and its alloys”, in *Fundamentals of Magnesium Alloy Metallurgy: A volume in Woodhead Publishing Series in Metals and Surface Engineering*, Elsevier Inc., 197-231, 2013.

- [20] Zhuang, H., Han, Y., Feng, A., “Preparation, mechanical properties and in vitro biodegradation of porous magnesium scaffolds”, *Materials Science and Engineering C*, 28(8): 1462–1466, (2008).
- [21] Yamashita, A., Horita, Z., Langdon, T. G., “Improving the mechanical properties of Magnesium and a Magnesium alloy through severe plastic deformation”, *Transactions of Nonferrous Metals Society of China*, 18(2): 309-314, 2001.
- [22] Myers, R.H., Montgomery, D.C., Anderson-Cook, C.M., “Response Surface Methodology”, Third Edition, John Wiley & Sons, New York, (2009).
- [23] Ferreira, S. L. C., Bruns, R. E., Ferreira, H.S., Matos, G. D., David, J. M., Brandão, G.C., da Silva, E.G.P., Portugal, L. A., dos Reis, P. S., Souza, A.S., dos Santos, W.N.L., “Box-Behnken design: An alternative for the optimization of analytical methods”, *Analytica Chimica Acta*, 597(2): 179-186, (2007).
- [24] Rios, J., Restrepo, A., Zuleta, A., Bolívar, F., Castaño, J., Correa, E., Echeverria, F., “Effect of ball size on the microstructure and morphology of mg powders processed by high-energy ball milling”, *Metals*, 11(10): 1621, (2021).
- [25] Fultz, B., Howe, J. M., Fultz, B., Howe, J. M., “Diffraction and the X-ray powder diffractometer”, *Transmission Electron Microscopy and Diffractometry of Materials*, 1-61, (2001).
- [26] Wang, F., Zhou, Q., Li, X. Z., Yoo, Y., Nastasi, M., Cui, B., “Electron microscopy observation of electric field-assisted sintering of stainless steel nanoparticles”, *Journal of Materials Science*, 56(3): 2584-2596, (2021).